





Pseudo-Bayesian Model-Based Noninvasive Intracranial Pressure Estimation and Tracking

Syed M. Imaduddin , *Student Member, IEEE*, Andrea Fanelli , *Member, IEEE*, Frederick W. Vonberg, Robert C. Tasker , and Thomas Heldt , *Senior Member, IEEE*

Abstract—Objective: A noninvasive intracranial pressure (ICP) estimation method is proposed that incorporates a model-based approach within a probabilistic framework to mitigate the effects of data and modeling uncertainties. **Methods:** A first-order model of the cerebral vasculature relates measured arterial blood pressure (ABP) and cerebral blood flow velocity (CBFV) to ICP. The model is driven by the ABP waveform and is solved for a range of mean ICP values to predict the CBFV waveform. The resulting errors between measured and predicted CBFV are transformed into likelihoods for each candidate ICP in two steps. First, a baseline ICP estimate is established over five data windows of 20 beats by combining the likelihoods with a prior distribution of the ICP to yield an *a posteriori* distribution whose median is taken as the baseline ICP estimate. A single-state model of cerebral autoregulatory dynamics is then employed in subsequent data windows to track changes in the baseline by combining ICP estimates obtained with a uniform prior belief and model-predicted ICP. For each data window, the estimated model parameters are also used to determine the ICP pulse pressure. **Results:** On a dataset of thirteen pediatric patients with a variety of pathological conditions requiring invasive ICP monitoring, the method yielded for mean ICP estimation a bias (mean error) of 0.6 mmHg and a root-mean-squared error of 3.7 mmHg. **Conclusion:** These performance characteristics are well within the acceptable range for clinical decision making. **Significance:**

The method proposed here constitutes a significant step towards robust, continuous, patient-specific noninvasive ICP determination.

Index Terms—Bayesian estimation, model-based signal processing, intracranial pressure, brain injury.

I. INTRODUCTION

INTRACRANIAL pressure (ICP) is the hydrostatic pressure of the cerebrospinal fluid (CSF). The normal mean ICP in healthy adults in the supine posture ranges from about 6 to 18 mmHg [1]–[3]. Its clinical importance derives from the fact that elevated ICP can impair brain tissue perfusion, possibly culminating in severe cerebral ischemic injury and brain herniation [4], [5]. Such ICP elevations can occur in a variety of neuropathological conditions that include hydrocephalus, traumatic brain injury (TBI), hemorrhagic stroke, and brain tumors [4]. Elevated ICPs are therefore treated aggressively in current clinical practice. The latest consensus guidelines for TBI care in adults recommend maintaining mean ICP below 22 mmHg [6] and in children below 20 mmHg [7].

Clinical ICP measurement modalities are invasive, require neurosurgical expertise, and carry an associated risk of infection [8], [9]. ICP monitoring is therefore used only for severely ill patients in spite of evidence that a larger pool of subjects may benefit from ICP assessment [10]. This potential need has prompted the development of noninvasive ICP (nICP) estimation approaches. Despite significant research effort, however, continuous nICP estimation has remained elusive and has not been adopted in clinical practice [11]. For intermittent ICP assessment, tympanic membrane displacement [12], optic nerve sheath distension [13], and application of external pressure on the eyeball to balance retro-orbital tissue pressure with ICP [14] have all been shown to correlate with ICP. Examples of proposed continuous nICP estimation methods include exploiting transcranial acoustic signal properties [15], [16], measuring cerebral blood flow velocity (CBFV) and calculating CBFV-derived indices [17], and measuring the arterial blood pressure (ABP) waveform and employing machine learning based methods using ABP and CBFV as inputs [18]–[20].

Recently, methods have been proposed to estimate mean ICP using mechanistic models of cerebrovascular physiology that relate cerebral blood flow (CBF), cerebral ABP (cABP), and ICP [21]–[26]. In practice, CBF and cABP are not measured, and these methods instead use CBFV and ABP measured at a peripheral location (pABP) as surrogates. These approxima-

Manuscript received June 29, 2019; revised August 1, 2019; accepted September 6, 2019. Date of publication September 13, 2019; date of current version May 20, 2020. This work was supported in part by the National Institutes for Neurological Disorders and Stroke of the United States National Institutes of Health under Grant R21 NS084264 and in part by Maxim Integrated Products and Philips Healthcare through funding to MIT's Medical Electronic Device Realization Center. The work of S. M. Imaduddin was supported by the Department of Electrical Engineering and Computer Science, Massachusetts Institute of Technology under the Grass Instruments Fellowship. (*Corresponding author: Thomas Heldt.*)

S. M. Imaduddin is with the Institute for Medical Engineering and Science, the Research Laboratory of Electronics, and the Department of Electrical Engineering and Computer Science, Massachusetts Institute of Technology.

A. Fanelli is with the Institute for Medical Engineering and Science and the Research Laboratory of Electronics, Massachusetts Institute of Technology.

F. W. Vonberg is with the Department of Anesthesiology, Critical Care and Pain Medicine, Boston Children's Hospital.

R. C. Tasker is with the Department of Anesthesiology, Critical Care and Pain Medicine and the Department of Neurology, Boston Children's Hospital.

T. Heldt is with the Institute for Medical Engineering and Science, the Research Laboratory of Electronics, and the Department of Electrical Engineering and Computer Science, Massachusetts Institute of Technology, Cambridge, MA 02139 USA (e-mail: thomas@mit.edu).

Digital Object Identifier 10.1109/TBME.2019.2940929

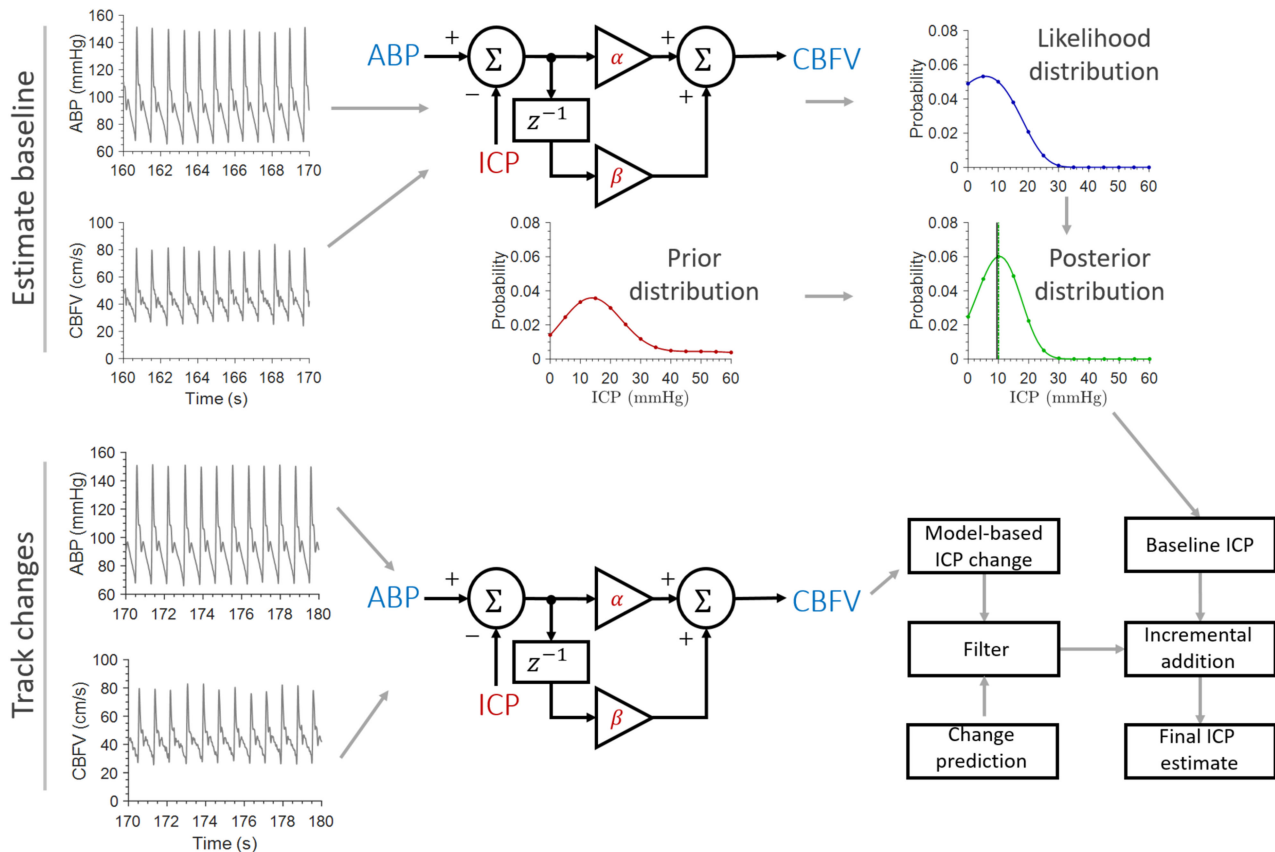


Fig. 1. Illustration of proposed method for mean nICP estimation. Arterial blood pressure (ABP) and cerebral blood flow velocity (CBFV) constitute the input waveforms. The ICP and two model parameters that represent cerebrovascular flow resistance and compliance, α and β , are then estimated. First, a baseline ICP is established by generating an *a posteriori* ICP distribution by combining a model-derived ICP likelihood distribution with a preselected prior belief. Model-derived changes in this baseline are subsequently filtered via predictions, and are added incrementally to the baseline to yield longitudinal ICP estimates.

tions, if not properly accounted for, can introduce errors in the estimated nICP because the ABP profile changes along the distributed arterial tree due to reflections from arterial branching sites and vessel taper [27]. Additionally, there is a physiological time delay between pABP and cABP due to the finite ABP wave propagation velocity as well as a time delay introduced by different bedside monitoring devices used to measure the ABP and CBFV waveforms [25]. Here we propose a probabilistic, model-based mean nICP estimation and tracking framework to reduce estimation sensitivity to such approximations. We then extend this framework to estimate the ICP pulse amplitude.

First, we estimate the mean ICP. To do so we represent cerebral hemodynamics as a first-order, time-varying system that relates cABP, mean ICP, and CBF, and model the temporal ICP evolution as a first-order autoregressive (AR) process. We use radial ABP (rABP) and CBFV as surrogates for cABP and CBF, respectively. Our method achieves resilience to the temporal misalignment via a Bayesian estimation framework, wherein we solve our model of cerebral hemodynamics for a physiologically plausible range of candidate ICP values and time offsets to form an ICP likelihood distribution. We combine this distribution with a prior belief about the patient's ICP and select the resulting posterior distribution's median as the baseline ICP. In addition, the likelihood distributions of each data window are

utilized to form estimates of the cerebrovascular flow resistance and compliance that are then used to estimate the ICP pulse pressure in a computationally simple and training-free manner. Subsequent changes in the mean ICP are computed with a uniform prior belief to reduce dependence on the initial prior distribution. The estimated ICP changes are further filtered via predictions obtained from the AR model of ICP dynamics for increased robustness.

We first present our nICP estimation method in Section II and describe our clinical data in Section III. We present and discuss our nICP estimation results on a cohort of thirteen pediatric patients in Sections IV and V, respectively, and provide concluding remarks in Section VI.

II. NONINVASIVE ICP ESTIMATION METHOD

We model the CBFV waveform as the output of a two-tap finite impulse response (FIR) filter whose input is the cerebral perfusion pressure (CPP) – the difference between cABP and ICP (Fig. 1). We neglect pulsatility in the ICP waveform, thus simplifying our task to estimating the filter taps (or model parameters) and the mean ICP value using measured rABP and CBFV. To do so, we subtract a range of physiologically plausible mean ICP values from the rABP signals to generate a set of

CPP waveforms. We then obtain estimates of the FIR filter taps for each CPP waveform by minimizing the associated CBFV prediction error in a least-square error sense. This is done for a range of time offsets between the CBFV and CPP signals. The CBFV prediction errors obtained for each candidate CPP and time offset pair are then transformed into a likelihood distribution of ICP values. Point estimates of this likelihood distribution (such as the mean or median) may then be taken as the final nICP estimates.

We employ this scheme in a two-stage process to increase the nICP estimation accuracy (Fig. 1). First, we establish a baseline nICP estimate and subsequently track changes in this value. To set the baseline, we combine the likelihood distribution with a preset prior belief of ICP values, and take the median of the resulting *a posteriori* distribution as the nICP estimate. This procedure is repeated for several data windows, and the nICP estimates are averaged together to yield the baseline. We employed a prior distribution that generously models ICP values encountered at the bedside – extremely high and low values are given significant weight – in order to ensure our method’s generalizability.

After this initial baseline estimation stage, subsequent nICP estimates are computed with a uniform distribution to reduce dependence on the initial prior belief. A downside of using a uniform distribution, however, is that the resulting nICP estimates are more prone to deviate from measured values. In our method, we addressed this problem by filtering changes in estimated nICP by model-predicted ICP changes via a Kalman filter-like approach [28], and subsequently adding the filtered nICP changes back to the baseline. We first describe our model of cerebral hemodynamics, before describing the associated estimation and tracking method.

A. Model of Cerebral Hemodynamics

We employed a discrete-time approximation of the two-element continuous-time model proposed earlier by our group [21], [23] with the addition of an AR process description of ICP evolution. For the m^{th} estimation window, this continuous-time model is of the form

$$q(t - t_0) = \frac{1}{R_m}(p_a(t) - p_i(t)) + C_m \frac{d}{dt}(p_a(t) - p_i(t)) \quad (1)$$

where q and p_a denote the CBFV and cABP, respectively (Fig. 2), and t_0 is an unknown time offset between *measured* CBFV and ABP. The time offset explicitly reflects the reality associated with measuring pABP and the model assuming cABP.

The resistive element, R_m , models resistance to cerebrovascular blood flow, while the capacitive element, C_m , represents the aggregate arterial and brain tissue compliance. The cerebral autoregulatory processes that modulate the resistance and compliance tend to occur over timescales longer than the data window lengths considered here [23], and hence both R_m and C_m are assumed constant over the duration of a data window, chosen to be 20 beats throughout this work.

We initially focus on estimating the mean ICP, $I[m]$, in the data window, and make the simplifying assumption that pulsatility

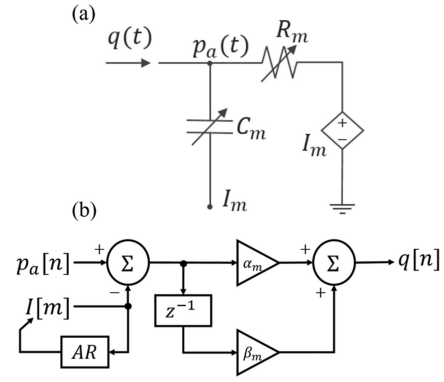


Fig. 2. (a) Continuous-time circuit model of cerebral hemodynamics proposed in [23]. We employed a discrete-time approximation of this model augmented with an AR process description of ICP evolution. (b) Discrete-time model of the cerebral vasculature. Samples of the cABP, p_a , and the CBFV, q , are related by a time-varying FIR filter, whose coefficients, α_m and β_m are assumed to remain constant during individual estimation windows. The mean ICP, $I[m]$, is also assumed to be constant during an estimation window, and its evolution is modeled by an AR process.

ity in the ICP waveform may initially be ignored. This leads to the simplified dynamic relationship

$$q(t - t_0) = \frac{1}{R_m}(p_a(t) - I[m]) + C_m \frac{d}{dt}(p_a(t) - I[m]) \quad (2)$$

where we have substituted the mean ICP, $I[m]$, for the ICP waveform and assume $I[m]$ to be constant over the duration of an estimation window. Approximating the derivative operation by first-order finite differences, and denoting the discrete-time sampling index with n , we obtain

$$\begin{aligned} q[n - d_0] &= \left(\frac{1}{R_m} + C_m f_s \right) (p_a[n] - I[m]) \\ &\quad - C_m f_s (p_a[n - 1] - I[m]) \\ &= \alpha_m (p_a[n] - I[m]) + \beta_m (p_a[n - 1] - I[m]) \end{aligned} \quad (3)$$

where f_s is the sampling rate, $\alpha_m = 1/R_m + C_m f_s$, $\beta_m = -C_m f_s$, and $d_0 = f_s \times t_0$. We chose first-order finite differences because cABP and CBFV are quasi-periodic signals, and their spectral content is concentrated around a few frequency harmonics, thus limiting the order of models whose parameters can be reliably estimated using only the cABP and CBFV [29]. Like their continuous-time counterparts, the model parameters α_m and β_m are assumed to remain constant during individual estimation windows.

We augmented this model with a first-order AR process to model inter-estimation-window temporal evolution of the mean ICP. This AR process is of the form

$$\Delta I[m] = \gamma_m \Delta I[m - 1] + v_m \quad (4)$$

where $\Delta I[m] = I[m] - I[m - 1]$ is the window-by-window difference in mean ICP, and v_m is a white-noise sequence with variance σ_v^2 . The parameter γ_m represents the autoregulatory state, with values of γ_m close to zero modeling static mean ICP values. In our method, we set $\gamma_m = 1$ to model rapidly changing

mean ICP values. Final mean nICP estimates are obtained by fusing noninvasive estimates of ΔI with predictions generated from this AR model.

The first-order system of (3), along with the ICP AR process description of (4), form our complete model of cerebral hemodynamics in the proposed mean nICP estimation method, and are summarized schematically in Fig. 2. This method comprises two stages that employ a common model-solving routine. We describe this routine next, and then proceed to describing the two stages. Finally, we describe how our model-based estimation routine can also be used to noninvasively estimate the ICP pulse pressure.

B. Model-Based Bayesian Estimation Routine

The model-based nICP estimation routine is employed in both baseline determination and subsequent nICP tracking, and it solves the model in (3) for a range of candidate ICP and time offset pairs. It takes as input rABP and CBFV signals in individual estimation windows, and computes nICP estimates by treating each window independently. Since all operations are confined to individual data windows, we omit the window index, m , for clarity in the remainder of this section.

We select the time offset range on a window-by-window basis such that, on average, the CBFV peaks are constrained to lead the corresponding rABP systolic peaks whilst ensuring that the diastolic points of the two waveforms are aligned with each other (Fig. 3). These imposed constraints are motivated by the underlying Windkessel-like model (Fig. 2a) that implies that both signals should start rising nearly simultaneously at the onset of systole, with the CBFV rising faster to reach its peak before the rABP. To compensate for inaccurate beat detections and modeling inaccuracies, we allowed the diastolic indices of the two waveforms to differ by at most three sampling intervals (≈ 25 ms). All time offsets that satisfy these two criteria are included in the time offset scan range.

To form the ICP scan range, we start scanning from an ICP of 0 mmHg in increments of 1 mmHg, a granularity deemed sufficient for clinical purposes. We stop at the mean rABP in the estimation window, as the ICP should not exceed the mean rABP itself. Negative ICP values are not considered here as they occur rarely [30], particularly in the pathologies of interest here.

For each ICP and time offset pair, we compute estimates for α and β in a least-square error sense

$$\begin{aligned} \left[\hat{\alpha}^{I,d}, \hat{\beta}^{I,d} \right]^T &= \left(\Phi^T \Phi \right)^\dagger \Phi^T \mathbf{q}^d \\ \text{where } \mathbf{q}^d &= [q[2-d], \dots, q[N-d]]^T \\ \Phi^I &= \begin{bmatrix} p_a[2] - I & p_a[1] - I \\ \vdots & \vdots \\ p_a[N] - I & p_a[N-1] - I \end{bmatrix} \end{aligned} \quad (5)$$

Here, the \dagger symbol represents a matrix pseudo-inverse, N denotes the number of samples in the estimation window, and I and d signify the solution's dependence on the candidate ICP and time offset values, respectively. Values for the cerebrovascular

flow resistance and compliance can be estimated according to

$$\begin{aligned} \hat{R}^{I,d} &= \left(\hat{\alpha}^{I,d} + \hat{\beta}^{I,d} \right)^{-1} \\ \hat{C}^{I,d} &= -\hat{\beta}^{I,d} / f_s \end{aligned} \quad (6)$$

The corresponding residual-error norm is given by

$$\zeta^{I,d} = \left\| \Phi^I \left[\hat{\alpha}^{I,d}, \hat{\beta}^{I,d} \right]^T - \mathbf{q}^d \right\|_2 \quad (7)$$

We define a likelihood distribution $\mathcal{L}(I, d)$ over the ICP and time offsets as

$$\begin{aligned} \mathcal{L}(I, d) &= \frac{1}{S_{\mathcal{L}}} \times \exp \left\{ - \left(\frac{\zeta^{I,d}}{\zeta_m} \right)^2 \right\} \\ \zeta_m &= \min_{I,d} \zeta^{I,d} \end{aligned} \quad (8)$$

where $S_{\mathcal{L}}$ is chosen so that $\mathcal{L}(I, d)$ normalizes to one. This formulation assigns a high likelihood to (I, d) pairs that result in a small residual CBFV prediction error, and a low likelihood to pairs with large residual error norms. To subsequently employ a prior distribution across the ICP, we marginalize $\mathcal{L}(I, d)$ across the time offsets to generate a one-dimensional likelihood distribution defined across ICP only

$$\mathcal{L}(I) = \sum_d \mathcal{L}(I, d) \quad (9)$$

An nICP estimate may be derived from the likelihood by computing a point statistic, \hat{I}_L , with an associated distribution variance, σ_L^2 . For our application here, $\hat{I}_L = \text{median}(\mathcal{L}(I))$. Finally, an *a posteriori* distribution is generated by combining the likelihood distribution with our prior belief

$$\Pr(I|p_a, q_v) = \frac{1}{S_P} \times \Pr(I) \mathcal{L}(I) \quad (10)$$

where $\Pr(I)$ is the prior belief and S_P is chosen so that the distribution normalizes to one. The median and variance of this combined distribution are denoted as \hat{I}_C and σ_C^2 , respectively.

In our method, we used both a uniform belief and a belief of the form

$$\Pr(I) = \begin{cases} \frac{1}{S} \times \sum_{k=1}^2 \frac{w_k}{\sqrt{2\pi}\sigma_k} \exp \left\{ -\frac{1}{2} \left(\frac{I - \mu_k}{\sigma_k} \right)^2 \right\}, & I \in I_{\text{range}} \\ 0, & I \notin I_{\text{range}} \end{cases}$$

$$w_1, w_2 \in [0, 1], \text{ subject to the constraint } w_1 + w_2 = 1 \quad (11)$$

where I_{range} denotes the ICP scan range, and S is chosen such that $\Pr(I)$ sums to unity.

We established the parameters of this distribution in a pilot exploration using 46 twenty-beat estimation windows from three subjects [31], and found the mean ICP and associated standard deviation to be 13.6 and 2.8 mmHg, respectively. We then set $\mu_1 = 13.6$ mmHg to model low ICP, and set $\sigma_1 = 10$ mmHg – a value larger than the ICP standard deviation in the 46 estimation windows – to model greater variation in ICP. Additionally, we set $\mu_2 = 50$ mmHg and $\sigma_2 = 20$ mmHg to model high ICP.

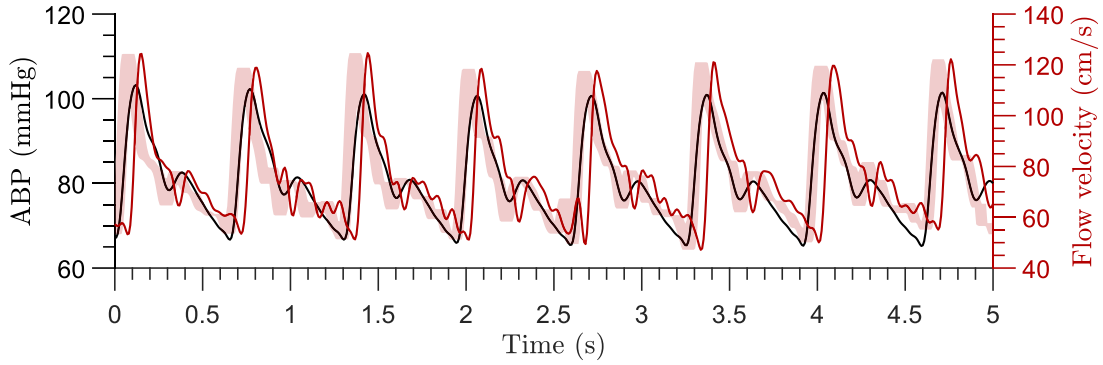


Fig. 3. Illustration of the time offset range. The input ABP and CBFV waveforms are plotted in black and red, respectively, and the range over which the CBFV signal is shifted is plotted as a red band.

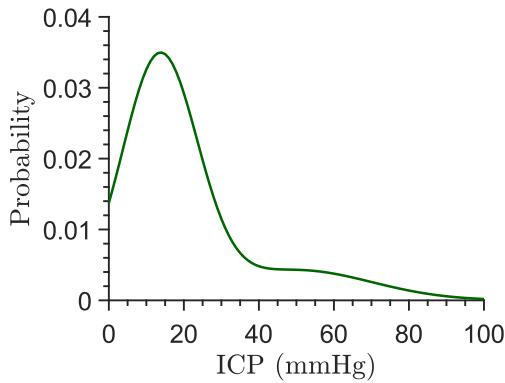


Fig. 4. Prior distribution used for baseline estimation. ICP values below 5 mmHg, as well as those exceeding 30 mmHg, have been assigned probabilities larger than that found in our data to make our method broadly applicable. The distribution is composed of a mixture of two truncated Gaussian distributions that model low and high ICP values.

We set $w_1 = 0.8$ and $w_2 = 0.2$, noting that the mean ICP exceeded 30 mmHg in 20% of the data reported in a previous study [23]. The resulting distribution is shown in Fig. 4.

C. Baseline nICP Estimation

To establish a baseline, we compute *a posteriori* nICP estimates, \hat{I}_C , in the first $M_b = 5$ twenty-beat data windows. These estimates are averaged to yield the baseline, \hat{I}_B . We set M_b to five to ensure that one hundred beats (normally more than a minute) of data are analyzed before setting the baseline.

The baseline ICP is then passed to the subsequent tracking stage. This stage uses the nICP estimates \hat{I}_L derived from the likelihood distribution alone. This amounts to using a uniform prior belief, and is done to reduce dependence on the initial prior distribution. Using a uniform belief, however, also increases the chances of erroneous nICP estimates. We therefore developed a tracking framework that filters the changes in nICP estimates computed with the uniform prior belief. This filtering is achieved by combining the changes in nICP estimates with model-predicted changes obtained with our AR process model.

D. Tracking Changes in the ICP

Filtered nICP-change estimates are computed by combining *model-predicted* changes in ICP with *noninvasively determined* window-by-window estimates of ICP change. The latter are computed using the method in Section II-B with a uniform prior distribution, and are denoted as $\Delta L[m]$ to suggest their dependence on the nICP estimates \hat{I}_L derived from the likelihood distribution. Their associated variances are $\sigma_{\Delta L}^2[m]$. We denote the model-predicted ICP changes as $\Delta P[m]$. Their estimated variances are denoted as $\sigma_{\Delta P}^2[m]$. Likewise, the filtered nICP-change estimates are denoted as $\hat{\Delta I}[m]$ and their variance estimates as $\sigma_{\hat{\Delta I}}^2[m]$.

Assuming that likelihood distributions of successive estimation windows are statistically independent,

$$\Delta L[m] = \hat{I}_L[m] - \hat{I}_L[m-1]$$

$$\sigma_{\Delta L}^2[m] = \sigma_L^2[m] + \sigma_L^2[m-1] \quad (12)$$

The variance estimates are upper bounds on the true variances because, by virtue of the independence assumption, the covariance terms have not been included. We compensated for this by using relatively large values of σ_v^2 in (4). Next, we compute the model-predicted ICP change and its variance as

$$\Delta P[m] = \gamma_m \hat{\Delta I}[m-1]$$

$$\sigma_{\Delta P}^2[m] = \gamma_m^2 \sigma_{\hat{\Delta I}}^2[m-1] + \sigma_v^2 \quad (13)$$

where the prediction is made using the filtered change estimate, $\hat{\Delta I}[m-1]$, of the previous window. To initialize this computation at $m = M_b + 1$, we set $\hat{\Delta I}[M_b]$ and $\sigma_{\hat{\Delta I}}[M_b]$ to 0 mmHg.

Once both model-predicted and noninvasively determined ICP changes and their variances have been computed, they are combined such that

$$x = \frac{\sigma_{\Delta P}^2[m]}{\sigma_{\Delta P}^2[m] + \sigma_{\Delta L}^2[m]}$$

$$\sigma_{\hat{\Delta I}}^2[m] = x \sigma_{\Delta L}^2[m]$$

$$\hat{\Delta I}[m] = (1-x) \Delta P[m] + x \Delta L[m] \quad (14)$$

The resulting filtered change, $\widehat{\Delta I}[m]$, is added to $\widehat{I}[m-1]$ to yield the final nICP estimate,

$$\widehat{I}[m] = \widehat{I}[m-1] + \widehat{\Delta I}[m] \quad (15)$$

where the baseline, \widehat{I}_B , is used in the first iteration.

In this formulation, (14) can be seen to merge the model-predicted and noninvasively determined estimates of the window-by-window ICP change by assigning greater weight to the estimate with lesser variance. This Kalman-filter like process is repeated for subsequent estimation windows to yield nICP estimates with reduced dependence on the initial prior information.

E. Noninvasive ICP Pulse Pressure Estimation

The proposed pseudo-Bayesian approach generates a likelihood distribution, $\mathcal{L}(I, d)$, that may be used to determine *average* (window-by-window) values for the model parameters, α_m and β_m , or – equivalently – their continuous-time counterparts, R_m and C_m . These model parameters can then be used to estimate the average window-by-window ICP pulse pressure. The pulse pressure estimation procedure can be applied independently to each data window. In the following description we therefore again omit the window index, m . Then for each window, the expectation operator yields,

$$\begin{aligned} \bar{R} &= \sum_{I, d} \widehat{R}^{I, d} \cdot \mathcal{L}(I, d) \\ \bar{C} &= \sum_{I, d} \widehat{C}^{I, d} \cdot \mathcal{L}(I, d) \end{aligned} \quad (16)$$

where $\widehat{R}^{I, d}$ and $\widehat{C}^{I, d}$ are determined according to (6). Likewise, a window-by-window value for t_0 may be determined by choosing $\bar{t}_0 = \bar{d}_0/f_s$, where \bar{d}_0 is chosen to maximize $\mathcal{L}(I, d)$. Then, for mean-subtracted ABP, CBFV, and ICP waveforms, Eqn. (1) may be rewritten as

$$\tilde{q}(t - \bar{t}_0) = \frac{1}{\bar{R}} (\tilde{p}_a(t) - \tilde{p}_i(t)) + \bar{C} \frac{d}{dt} (\tilde{p}_a(t) - \tilde{p}_i(t)) \quad (17)$$

where $\tilde{q}(t)$, $\tilde{p}_a(t)$, and $\tilde{p}_i(t)$ are mean-subtracted CBFV, ABP, ICP, respectively. Taking Fourier transforms and rearranging the equation yields

$$\tilde{P}_i(j\Omega) = \tilde{P}_a(j\Omega) - \frac{\bar{R} \cdot e^{-j\Omega \bar{t}_0}}{1 + j\Omega \bar{R} \bar{C}} \tilde{Q}(j\Omega) \quad (18)$$

where $\tilde{Q}(j\Omega)$, $\tilde{P}_a(j\Omega)$, and $\tilde{P}_i(j\Omega)$ are the Fourier transforms of $\tilde{q}(t)$, $\tilde{p}_a(t)$, and $\tilde{p}_i(t)$, respectively, and Ω is the radial frequency. We first determine representative wavelets for $\tilde{q}(t)$ and $\tilde{p}_a(t)$ in each data window by averaging over the individual heartbeats in that window while maintaining a common length across each heartbeat. This common length is set to the smallest beat duration in the ABP data, and beats exceeding this length are clipped. We then compute the discrete Fourier transform (DFT) of the wavelets with the transform length set to the number of samples in the wavelets. Doing so amounts to performing a discrete Fourier series decomposition of periodic signals formed by the ABP and CBFV wavelets with each DFT bin corresponding to a frequency harmonic [32]. $\tilde{P}_i(j\Omega)$ can thus be evaluated at the

TABLE I
PATIENT INFORMATION

Subject	Diagnosis	Recording sessions	Duration (hr:min)	[Min., Max.] ICP (mmHg)
1	Stroke	11	2:02	[9, 22]
2	Traumatic brain injury	6	0:44	[5, 9]
3	Stroke	2	0:21	[7, 12]
4	Hemorrhage	2	0:25	[8, 16]
5	Brain tumor	3	0:09	[5, 11]
6	Intraventricular hemorrhage	4	0:26	[8, 25]
7	Hydrocephalus	3	0:27	[8, 20]
8	Traumatic brain injury	1	0:08	[6, 14]
9	Traumatic brain injury	4	0:41	[4, 21]
10	Hydrancephaly/ Hydrocephalus	1	0:01	[7, 7]
11	Cerebro-hepatopathy	2	0:34	[1, 16]
12	Cavernous malformation	2	0:31	[4, 8]
13	Chiari malformation	1	0:10	[4, 13]
Ensemble		42	6:40	[1, 25]

frequency harmonics by using the DFT output in conjunction with Eqn. (18) such that

$$\tilde{P}_i(jh\Omega_0) = \tilde{P}_a(jh\Omega_0) - \frac{\bar{R} \cdot e^{-jh\Omega_0 \bar{t}_0}}{1 + jh\Omega_0 \bar{R} \bar{C}} \tilde{Q}(jh\Omega_0) \quad (19)$$

where $h = \pm 1, \pm 2, \dots$ indicates the frequency harmonic, $\Omega_0 = 2\pi f_s/M$ is the continuous-time periodic frequency for a repeating wavelet of M samples, and $\tilde{P}_a(jh\Omega_0)$ and $\tilde{Q}(jh\Omega_0)$ are set to the h^{th} DFT bins of the ABP and CBFV wavelets, respectively. Noise and modeling inaccuracies mean that reliable estimates may not be available for higher harmonics. Instead of fixing the number of harmonics to estimate, we applied a heuristic scheme that enforces monotonicity in the spectral estimates by retaining only those harmonics whose spectral magnitude is below the preceding harmonics. Once the harmonics have been selected, the inverse DFT is used to obtain an approximate reconstruction of an ICP wavelet.

III. DATA COLLECTION AND PREPROCESSING

We used data collected at Boston Children's Hospital (BCH) between February 2015 and June 2017 as previously reported in [25]. Briefly, the data collection protocols were approved by the Institutional Review Boards at BCH and MIT, and informed consent was obtained from patients or their surrogates prior to data collection. Individual recording sessions typically lasted for nearly twenty minutes during which the rABP, CBFV, and (invasive) ICP waveforms were recorded simultaneously. Important metadata, including height differences between the location of ICP and rABP transducers, were also recorded. Data were included from thirteen patients (4 females, 9 males, aged between 2–25 years with a median age of 11 years) who presented with different pathologies including TBI, hydrocephalus, and hemorrhagic strokes with ICP values ranging from 1 to 25 mmHg. The patient information is further summarized in Table I.

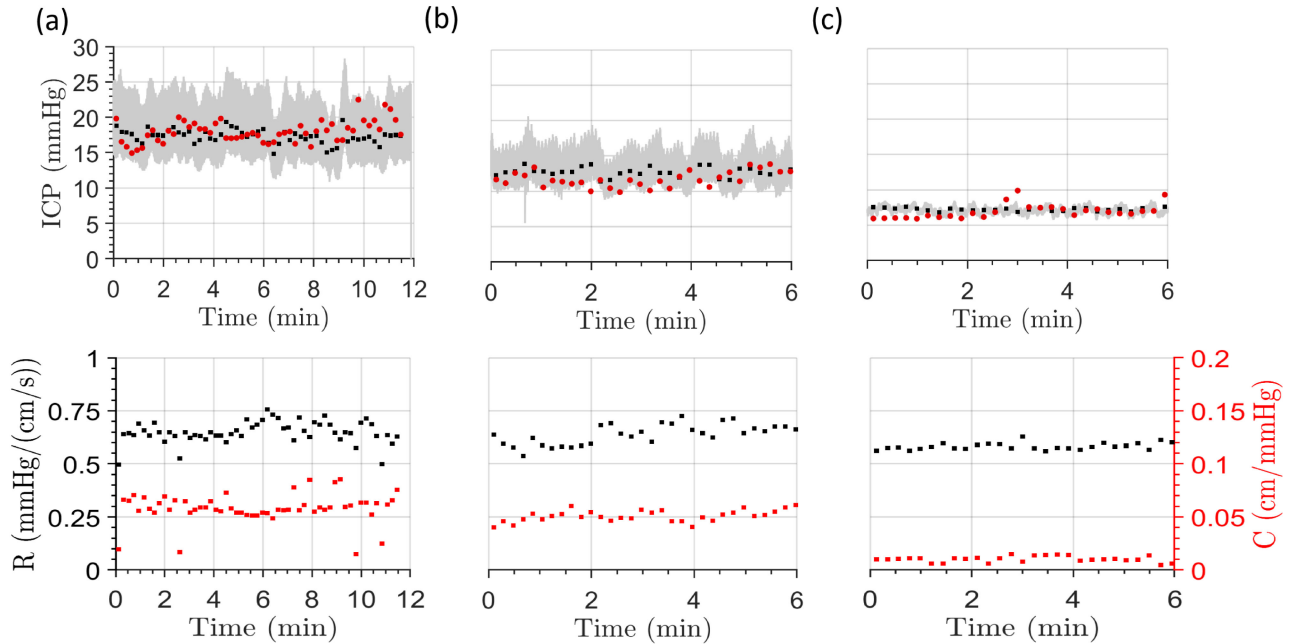


Fig. 5. Three examples of nICP, resistance, and compliance estimates. Top panel: Invasive reference ICP measurements are shown in gray. Window-by-window average of the reference ICP and nICP values are in black and red, respectively. The nICP estimates had a bias of 0.7, -1.0 , and -0.3 mmHg, standard deviation of error of 1.9, 1.4, and 1.1 mmHg, and RMSE of 2.0, 1.7, and 1.1 mmHg, respectively. Bottom panel: Resistance (black) and compliance (red) estimates.

We tested our method's performance on clean data segments extracted from the ensemble data. Details of the segment extraction process are presented elsewhere [25]. Briefly, CBFV and rABP waveform quality was assessed, and segments of noisy data were removed before applying a coarse time-alignment step between the rABP and the CBFV signals to account – on average – for time delays introduced by different measurement devices. This was done by computing the cross-correlation between rABP and CBFV signals, and selecting the lag with the highest cross-correlation coefficient as the desired offset. The signals were then resampled to a common 125 Hz to compensate for any underlying sampling frequency discrepancies. Finally, the baseline rABP was adjusted to account for differences in ICP and rABP transducer heights as suggested previously in [24].

In contrast to [25], we passed the resulting six hours and forty minutes of data through an out-of-band-noise removal stage. The rABP and CBFV trends were first extracted via a moving-average filter. These trends were subtracted from the rABP and CBFV signals, respectively, and the resulting detrended signals were filtered by a bandpass filter with cutoffs at 0.5 and 16 Hz. The trend removed in the first stage was then added back to the filter output to restore the original DC levels. The filtered data were then passed to our estimation routine that computed nICP estimates in non-overlapping twenty-beat windows.

IV. ICP ESTIMATION RESULTS

Nearly seven hours of data (1,657 twenty-beat nonoverlapping estimation windows) were analyzed, and estimates were computed in a fully automated manner for reproducibility. The

results were computed by setting $\sigma_v = 15$ mmHg for the model in (4) to model rapidly changing ICPs. This was done to ensure our method's generalizability to diverse datasets [31].

Representative examples of the estimation results are shown in Fig. 5. These recordings indicate that our method can generate nICP estimates that are within clinically acceptable accuracy compared to standard invasive methods.

Bland-Altman analysis [33] on a per-estimation-window basis (Fig. 6) indicates that our method achieved a mean error (bias) of 0.6 mmHg and RMSE of 3.7 mmHg across the 1,657 ICP-to-nICP comparisons, with associated limits of agreement (bias ± 1.96 standard deviation (SD)) of -6.6 to 7.7 mmHg, respectively. Likewise, the comparison on a per-recording basis revealed an estimation bias and RMSE of 0.8 and 3.3 mmHg, respectively, with limits of agreement of -5.5 to 7.1 mmHg.

To further gauge our method's performance, we computed the fraction of nICP estimates below a certain RMSE on a per-record, per-estimation-window, and per-patient basis. This analysis is illustrated in Fig. 8 and indicates that nearly 80% of all our nICP estimates were within ± 5 mmHg of the invasive reference ICP measurements, indicating a strong agreement between invasive reference and noninvasive estimates.

While not a measure of agreement of two candidate measurement approaches [33], the correlation coefficient has historically been cited in studies on nICP estimation. Here, we achieved a correlation coefficient of 0.64 for the per-record analysis (Fig. 9). Given the comparatively small SD achieved in our nICP estimates, the value of the correlation coefficient seems limited by the limited range of measured ICP values, rather than pointing to a limitation of the estimation approach [23], [33].

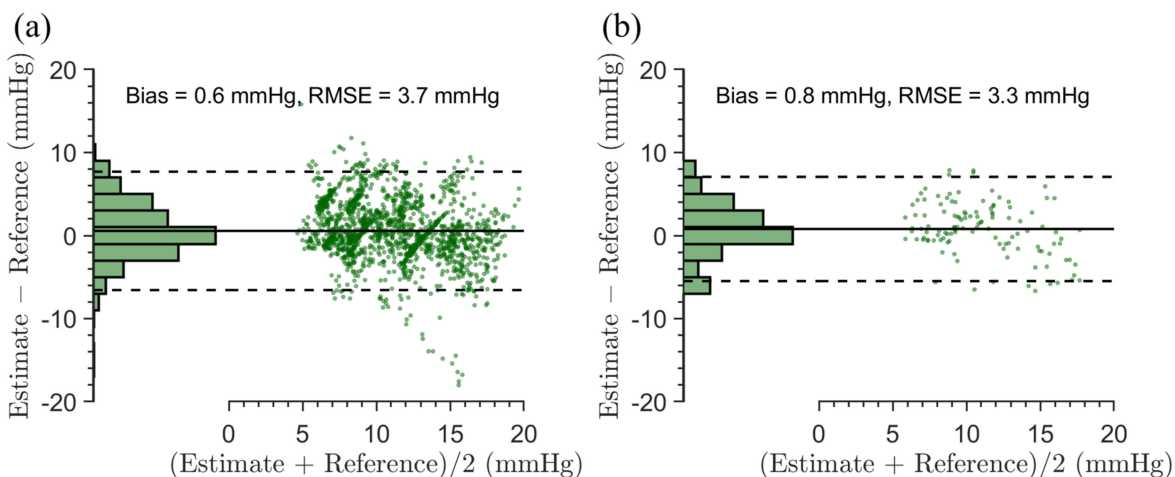


Fig. 6. Bland-Altman analysis of estimation performance on (a) per-estimation-window and (b) per-recording-window bases. Solid lines indicate the bias (mean error); dashed lines are the limits of agreement computed as bias \pm 1.96 \times SD.

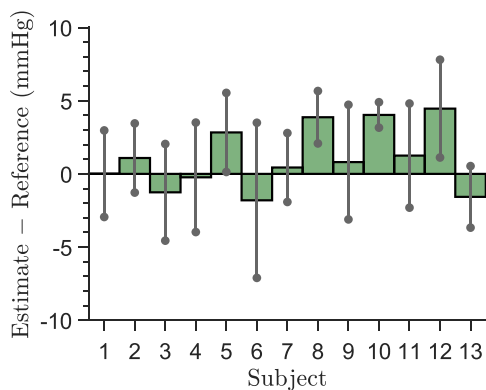


Fig. 7. Estimation performance across all thirteen patients. Bars indicate the estimation bias; the unit standard deviations are shown in gray.

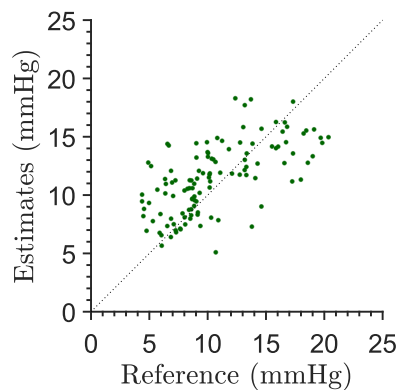


Fig. 9. Scatter plot of measured reference and estimated ICP on a per-record basis. A correlation coefficient of 0.64 was achieved.

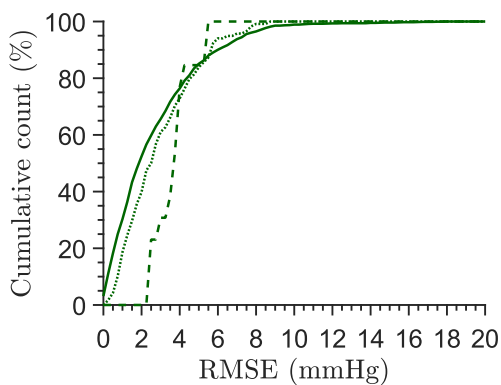


Fig. 8. Fraction of nICP estimates below a specified RMSE in per-estimation-window (solid), per-record (dotted), and per-patient (dashed) bases.

To assess our method’s performance in the absence of prior information about the ICP, we computed nICP estimates with a uniform prior distribution. The estimation performance is summarized in Table II, and shows that while the estimation

TABLE II
ESTIMATION ACCURACY

Configuration		(Bias, SDE, RMSE)
Prior distribution	Tracking	(mmHg)
Gaussian mixture	Yes	(0.6, 3.6, 3.7)
Gaussian mixture	No	(0.9, 3.8, 3.9)
Uniform	Yes	(1.0, 4.8, 4.9)
Uniform	No	(1.2, 5.0, 5.2)

accuracy decreased, the degree of degradation is not severe enough to render the estimates clinically unusable. Furthermore, we also computed the estimation accuracy by disabling the scans over multiple time offsets. The results are summarized in Table III and indicate that scanning over time offsets leads to improved accuracy with and without the Gaussian mixture prior distribution, although the effect is more pronounced when using a uniform prior distribution.

TABLE III
EFFECT OF NOT SCANNING OVER TIME OFFSETS

Configuration		(Bias, SDE, RMSE) (mmHg)
Prior distribution	Tracking	
Gaussian mixture	Yes	(1.5, 3.9, 4.2)
Gaussian mixture	No	(1.8, 4.0, 4.4)
Uniform	Yes	(2.7, 5.9, 6.5)
Uniform	No	(2.9, 6.2, 6.8)

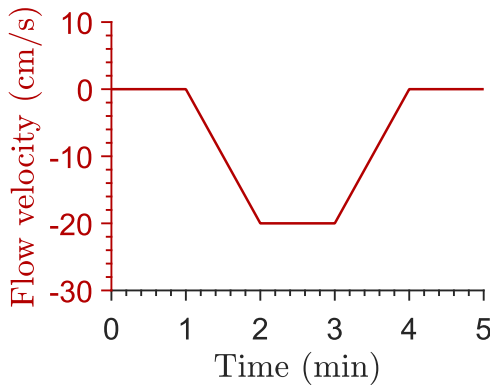


Fig. 10. Synthetic trend added to CBFV waveforms to determine efficacy of the tracking scheme.

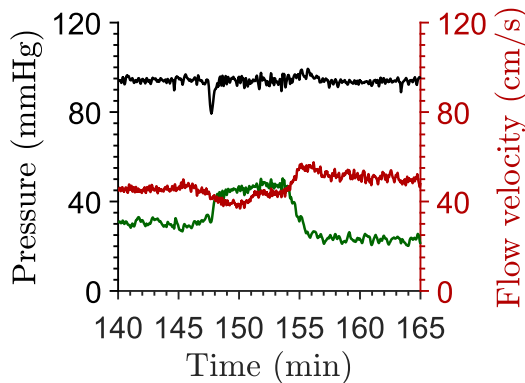


Fig. 11. Example of a plateau wave. Mean ABP (black), CBFV (red), and ICP (green) are shown. Rise in ICP is accompanied by a drop in mean CBFV while the mean ABP remains relatively stable. Data courtesy of Professor Marek Czosnyka, Department of Clinical Neurosciences, Addenbrooke's Hospital, University of Cambridge.

To test the tracking scheme's ability to follow transient changes, we added a synthetic trend to the CBFV signals and recomputed nICP estimates with the modified CBFV, whilst leaving the ABP waveforms unchanged. The synthetic trend is shown in Fig. 10, and we expected the nICP to increase in response, thereby mimicking plateau waves [34] (see Fig. 11 for an example of a plateau wave recorded in a clinical setting). Such plateau waves did not occur in our data. Estimates were computed both with tracking and with a static prior distribution applied to all data windows in data segments whose duration was

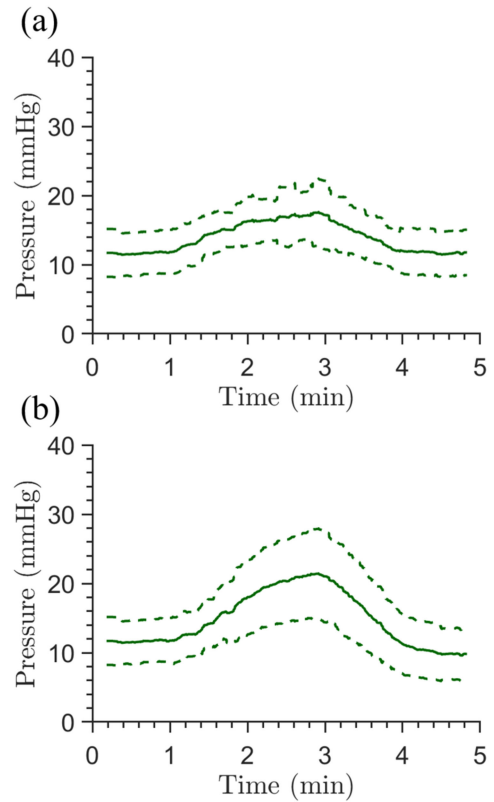


Fig. 12. Mean (solid) and unit SD bounds (dashed) of nICP estimates obtained with synthetic trend in CBFV (a) without and (b) with tracking.

longer than that of the five-minute synthetic trend. The mean and unit SD bounds of the resulting nICP estimates are shown in Fig. 12. The figure demonstrates that enabling the tracking scheme led to estimating greater transient changes than with a static prior distribution.

ICP pulse pressure estimation – Reference invasive ICP waveforms recorded with open external drain were excluded in this analysis since the pulsatility of those waveforms was damped due to exposure to atmospheric pressure. This resulted in 1093 20-beat data windows, or 4 hours of data. Distributions of differences between the measured and noninvasively determined ICP pulse pressure are shown in Fig. 13. On average, our noninvasively determined ICP pulse pressures had a bias of -1.2 mmHg, a SD of 3.8 mmHg, and a RMSE of 4.0 mmHg, suggesting that our estimates were close to invasively determined values, albeit on a small dataset.

V. DISCUSSION

Comparison with invasive ICP measurement modalities – Invasive ICP monitoring modalities include external ventricular drains (EVDs), commonly regarded as the clinical gold standard, integrated (micro-transducer) parenchymal sensing devices, such as the Camino or Codman sensors, and epi- or sub-dural pressure measurement probes. The latter are considered less reliable compared to parenchymal devices [11], [35], [36] and have largely been discontinued in neurocritical care. Performance analyses of parenchymal micro-transducers have

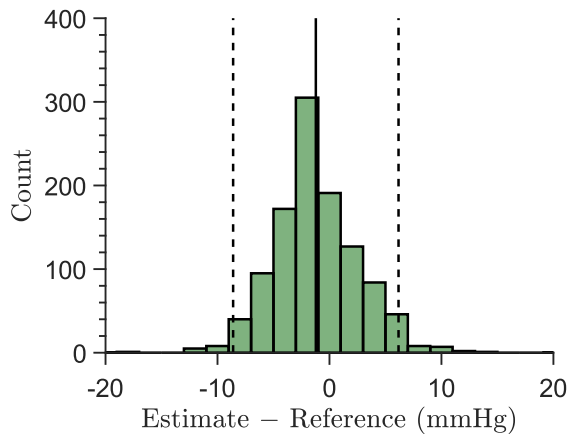


Fig. 13. Distribution of differences between estimated and reference ICP pulse pressure per estimation window. The bias (solid line) is -1.2 mmHg and 2 SD limits (dashed lines) are -8.8 mmHg and 6.4 mmHg.

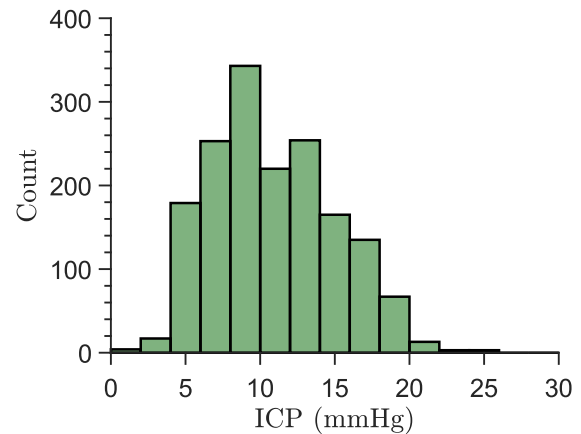


Fig. 14. Histogram of reference ICP values across all estimation windows in our data.

also been reported in the literature [11]. Lescot *et al.* [37], for example, reported that in a cohort of fifteen patients, the Codman sensor had an ensemble bias of 0.3 mmHg with limits of agreement of -6.7 and 7.1 mmHg, relative to simultaneous EVD measurements. Other studies reported similar performance metrics for two simultaneous invasive ICP measurements [38]. Our system achieved comparable performance characteristics (bias of 0.6 mmHg and limits of agreement of -6.6 and 7.7 mmHg).

Radial ABP measurement was the only (minimally) invasive aspect of our approach and was used because these measurements are readily available at the bedside in neurocritical care. The risk of infection from arterial catheters is reported to be far less than that associated with EVDs. O'Horo *et al.* [39], for instance, have reported infection rates of 1.5% in femoral arterial lines with 1.9 times greater risk of infection at femoral sites compared to radial sites. In contrast, infection rates of 5% [8] and 10% [9] have been previously reported in EVDs. Thus, our approach has a potentially lower risk of infection than invasive ICP measurement methods. Future use of noninvasive ABP monitors will eliminate any residual infection risks associated with our method [31].

ICP pulse pressure estimation – The obtained results indicate that our noninvasive procedure may also be used to determine ICP pulsatility. The slight negative ICP pulse pressure estimation bias may be attributed to estimation of limited, often fewer than two, harmonics. The estimation procedure, however, is training-free since it uses the likelihood distribution (instead of the posterior distribution) in a model-based fashion. It involves elementary computations and can thus be implemented in real-time with minimum computational burden. Since a variable number of harmonics are estimated per data window, it is not always possible to conduct a thorough analysis of the waveform morphology.

Other attempts of noninvasive determination of ICP pulsatility include the use of transcranial acoustic signals in conjunction with pretrained statistical models [15], use of pretrained transfer functions between ICP and aortic blood pressure [40],

and application of an iterative ensemble Kalman filter to a multiscale model of intracranial dynamics [26]. These approaches involve use of pre-trained models and associated parameters that may not generalize over larger patient populations. The pulse pressure information obtained from our method, in contrast, does not involve pre-training.

Features of our approach – Our proposed method yields accurate and patient-specific nICP estimates by combining a simple model of cerebral hemodynamics with an easily interpretable prior distribution of ICP values in a realtime, computationally straightforward manner. Doing so obviates the need to employ sophisticated multi-parameter models that describe complex cerebrovascular behaviors [41], [42] whose parameters are difficult to identify in a simple, noninvasive, robust, and patient-specific manner. Likewise, our proposed approach bypasses the need to resort to statistical learning frameworks that require rich datasets across a multitude of clinical conditions for robust training.

The proposed estimation framework differs from classical Bayesian system identification approaches that utilize iterative Markov chain Monte Carlo methods (see [43], [44]) and that may therefore not be feasible for real-time computation. Moreover, our prediction model allows for a simple method to fuse predicted and observed ICP changes. More sophisticated prediction models may be used. Increasing the complexity, however, may come at the cost of more computationally involved fusion methods.

We employed a prior distribution that only coarsely represents the ICP values in our dataset (see Fig. 14). Notably, we assigned greater probabilities to ICP values both below 5 mmHg and above 30 mmHg than the actual proportion of such values in our data. That our approach still achieved an RMSE below 4 mmHg is therefore highly encouraging. To us, this indicates that our method can potentially yield comparable accuracy to invasive measurements when some prior information about subjects' ICP ranges can be provided to the system. The system's performance in absence of prior information does not degrade significantly, as is indicated by the results achieved with a uniform prior distribution. This points towards the method's applicability to

cases where no *a priori* information may be available about patients' ICP values.

At present, we have employed a simplistic model of temporal ICP evolution. Filtering our ICP change estimates using predictions from this model yielded improved performance, whilst simultaneously relieving dependence on the initial prior distribution. The reduced dependence on the initial prior information will be important in monitoring subjects' ICP over long durations, and through large swings of ICP, as indicated by Fig. 12.

Kashif *et al.* [23] previously proposed the two-element continuous-time ICP model used here, and also developed an associated nICP estimation scheme. The authors reported an ensemble bias of 1.6 mmHg with an SDE of 7.6 mmHg in data from TBI patients with significant underlying ICP variability. They also averaged the nICP estimates obtained from CBFV signals recorded simultaneously from left and right middle cerebral arteries, and reported that this averaging resulted in a reduced SDE of 5.9 mmHg. They were, however, unable to account for the hydrostatic pressure offset between rABP and ICP measurements as they analyzed archived data and did not have access to the height differences between the ICP and rABP pressure transducers. Also, their data were recorded solely from adult TBI patients. Building on this work, Fanelli *et al.* [25] introduced an automated signal quality assessment stage in the model-based estimation scheme of Kashif *et al.* and automated all pre-processing steps, including time-alignment of the ABP and CBFV waveforms. Their method, however, still remained sensitive to temporal alignment of the input waveforms. They collected data from a heterogeneous pediatric patient population and reported nICP estimation bias and RMSE of 1.0 mmHg and 5.2 mmHg, respectively.

Our method differs from these prior approaches in several aspects. Sensitivity to time alignment is overcome by forming a likelihood distribution over several time offsets. Our method includes a strategy to take prior information about a subject's ICP into account whilst retaining the interpretability and computational simplicity afforded by the Kashif model. We incorporate temporal evolution of the mean ICP via our tracking framework – a facility not afforded by the previous work. While we did not have access to simultaneous bilateral CBFV recordings, our method might achieve better performance characteristics in such scenarios if averaging similar to that used by Kashif *et al.* were applied. We demonstrate that estimates of the mean ICP can be obtained with accuracies approaching those of gold-standard invasive methods. Moreover, our proposed method also determines the ICP pulse pressures noninvasively, in a training-free manner – a feature not previously developed in the prior work.

Contributions – The contributions of this present work include developing a model-based nICP estimation framework that encounters unknown physiologically-induced time offsets between rABP and CBFV signals. An attractive feature of our approach is that it retains its interpretability due to the underlying physiologic model – a facility not provided by pure statistical learning approaches to nICP estimation. Additionally, we have introduced a simple AR model of ICP dynamics that helps in tracking ICPs over long recording durations without overly relying on the prior distribution employed in the initial stage of the

method. For each data window, our method generates a probability distribution of ICP values, that can potentially be used to determine estimation-confidence metrics. We demonstrate that the likelihood distribution can also be used to determine estimates of the ICP pulse pressure in a patient-specific manner. Our system does not require calibration to invasive ICP measurements. It can thus be used as a screening tool for identifying patients suffering from elevated ICP without resorting to invasive procedures such as lumbar punctures.

In addition to monitoring patients suffering from neurological diseases, our approach can also be useful in monitoring intra-operative cerebral perfusion and autoregulation, for example. Both inadequate and excessive cerebral perfusion during surgical procedures has been shown to be a cause of post-operative delirium [45]. Surgical procedures such as coronary artery bypass grafting typically do not employ concurrent invasive ICP monitoring, and thus CPP cannot be directly measured. CPP derived from our nICP estimates can potentially be used to ameliorate this problem. Such clinical translation of our method will require implementing it for real-time operation. This is a feasible prospect because the method employs a set of deterministic, causal mathematical operations.

Limitations and future work – At present, we used a preset prior distribution. However, in a clinical scenario, physicians could be allowed to modify the distribution at the bedside using their insight. Additional work may focus on testing our proposed method on a larger dataset comprising subjects with additional pathologies and larger variations and transient changes in ICP. We have used routinely measured rABP recordings for estimating ICPs in our clinical dataset, and future validation of the method could also involve noninvasive blood pressure monitors. Work may also focus on harnessing information in the estimated model coefficients, α_m and β_m , or equivalently R_m and C_m , both for monitoring a subject's cerebral autoregulation status, and for assessing nICP estimation confidence on a window-by-window basis.

VI. CONCLUSION

Continuous nICP estimation can benefit a large number of patients that have traditionally been excluded from ICP monitoring due to the current invasiveness of the measurement. The nICP estimation framework proposed in this paper attempts to overcome challenges associated with model-based nICP estimation methods. Several possible time offsets between the rABP and CBFV are considered, which helps address the challenge posed by unknown (and patient-specific) time offsets between these signals. Estimation is performed within a Bayesian framework, which helps increase the method's resilience to structured errors that may be introduced, for instance, by differences between rABP and cABP morphology, and also to unstructured errors due to signal noise and motion artifacts in recorded data. Moreover, ICP pulse pressure amplitudes are determined in a patient-specific manner. It is hoped that this work will pave the way towards developing a reliable, continuous, realtime, accurate, and fully noninvasive ICP monitoring device to improve neurocritical care across the world.

ACKNOWLEDGMENT

MIT filed an invention disclosure covering the estimation framework in May 2018, listing S. M. Imaduddin, A. Fanelli, and T. Heldt as co-inventors.

REFERENCES

- [1] O. Gilland, "Normal cerebrospinal-fluid pressure," *New England J. Med.*, vol. 280, no. 16, pp. 904–905, 1969.
- [2] O. Gilland *et al.*, "Normal cerebrospinal fluid pressure," *J. Neurosurg.*, vol. 40, no. 5, pp. 587–593, 1974.
- [3] R. A. Avery *et al.*, "Reference range for cerebrospinal fluid opening pressure in children," *New England J. Med.*, vol. 363, no. 9, pp. 891–893, 2010.
- [4] L. A. Steiner and P. J. D. Andrews, "Monitoring the injured brain: ICP and CBF," *Brit. J. Anaesthesia*, vol. 97, no. 1, pp. 26–38, 2006.
- [5] C. Hawthorne and I. Piper, "Monitoring of intracranial pressure in patients with traumatic brain injury," *Frontiers Neurol.*, vol. 5, 2014, Art. no. 121.
- [6] N. Carney *et al.*, "Guidelines for the management of severe traumatic brain injury, fourth edition," *Neurosurgery*, vol. 80, no. 1, pp. 6–15, 2017.
- [7] P. M. Kochanek *et al.*, "Guidelines for the management of pediatric severe traumatic brain injury, third edition: Update of the brain trauma foundation guidelines, executive summary," *Pediatric Crit. Care Med.*, vol. 20, no. 2, pp. 280–289, 2019.
- [8] C. Weigand and P. Richards, "Measurement of intracranial pressure in children: A critical review of current methods," *Develop. Med. Child Neurol.*, vol. 49, no. 12, pp. 935–941, 2007.
- [9] H. I. Fried *et al.*, "The insertion and management of external ventricular drains: An evidence-based consensus statement," *Neurocrit. Care*, vol. 24, no. 1, pp. 61–81, 2016.
- [10] R. D. Simone *et al.*, "Intracranial pressure in unresponsive chronic migraine," *J. Neurol.*, vol. 261, no. 7, pp. 1365–1373, 2014.
- [11] X. Zhang *et al.*, "Invasive and noninvasive means of measuring intracranial pressure: A review," *Physiol. Meas.*, vol. 38, no. 8, pp. 143–182, 2017.
- [12] A. Reid *et al.*, "Mean intracranial pressure monitoring by a non-invasive audiological technique: A pilot study," *J. Neurol. Neurosurg. Psychiatry*, vol. 52, no. 5, pp. 610–612, 1989.
- [13] V. Rajajee *et al.*, "Optic nerve ultrasound for the detection of raised intracranial pressure," *Neurocrit. Care*, vol. 15, no. 3, pp. 506–515, 2011.
- [14] A. Ragauskas *et al.*, "Innovative non-invasive method for absolute intracranial pressure measurement without calibration," *Acta Neurochirurgica Suppl.*, vol. 95, pp. 357–361, 2005.
- [15] A. Levinsky *et al.*, "Non-invasive estimation of static and pulsatile intracranial pressure from transcranial acoustic signals," *Med. Eng. Phys.*, vol. 38, no. 5, pp. 477–484, 2016.
- [16] O. Ganslandt *et al.*, "Evaluation of a novel noninvasive ICP monitoring device in patients undergoing invasive ICP monitoring: Preliminary results," *J. Neurosurg.*, vol. 128, no. 6, pp. 1653–1660, 2018.
- [17] P. W. Hanlo *et al.*, "Monitoring intracranial dynamics by transcranial Doppler—A new Doppler index: Trans systolic time," *Ultrasound Med. Biol.*, vol. 21, no. 5, pp. 613–621, 1995.
- [18] B. Schmidt *et al.*, "Noninvasive prediction of intracranial pressure curves using transcranial doppler ultrasonography and blood pressure curves," *Stroke*, vol. 28, no. 12, pp. 2465–2472, 1997.
- [19] X. Hu *et al.*, "A data mining framework of noninvasive intracranial pressure assessment," *Biomed. Signal Process. Control*, vol. 1, no. 1, pp. 64–77, 2006.
- [20] P. Xu *et al.*, "Improved noninvasive intracranial pressure assessment with nonlinear kernel regression," *IEEE Trans. Inf. Technol. Biomed.*, vol. 14, no. 4, pp. 971–978, Jul. 2010.
- [21] F. M. Kashif *et al.*, "Model-based estimation of intracranial pressure and cerebrovascular autoregulation," *Comput. Cardiol.*, vol. 45, pp. 369–372, 2008.
- [22] X. Hu *et al.*, "Estimation of hidden state variables of the intracranial system using constrained nonlinear Kalman filters," *IEEE Trans. Biomed. Eng.*, vol. 54, no. 4, pp. 597–610, Apr. 2007.
- [23] F. M. Kashif *et al.*, "Model-based noninvasive estimation of intracranial pressure from cerebral blood flow velocity and arterial pressure," *Sci. Transl. Med.*, vol. 4, no. 129, pp. 129–144, 2012.
- [24] J. Noraky *et al.*, "Noninvasive intracranial pressure estimation in patients with subarachnoid hemorrhage," *Acta Neurochirurgica Suppl.*, vol. 122, pp. 65–68, 2016.
- [25] A. Fanelli *et al.*, "Fully automated, real-time, calibration-free, noninvasive intracranial pressure estimation," *J. Neurosurg., Pediatric*, vol. 24, no. 5, 2019.
- [26] J.-X. Wang *et al.*, "Data-augmented modeling of intracranial pressure," *Ann. Biomed. Eng.*, vol. 47, no. 3, pp. 714–730, 2019.
- [27] W. W. Nichols *et al.*, *McDonald's Blood Flow in Arteries, Sixth Edition: Theoretical, Experimental and Clinical Principles*. Boca Raton, FL, USA: CRC Press, 2011.
- [28] J. L. Speyer and W. H. Chung, *Stochastic Processes, Estimation and Control*. Philadelphia, PA, USA: SIAM, 2008.
- [29] L. Ljung, *System Identification – Theory for the User*. Englewood Cliffs, NJ, USA: Prentice-Hall, 1999.
- [30] A. S. Filippidis *et al.*, "Negative-pressure and low-pressure hydrocephalus: The role of cerebrospinal fluid leaks resulting from surgical approaches to the cranial base," *J. Neurosurg.*, vol. 115, no. 5, pp. 1031–1037, 2011.
- [31] S. M. Imaduddin, "A pseudo-Bayesian model-based approach for non-invasive intracranial pressure estimation," S.M. thesis, Dept. Elect. Eng. Comput. Sci., Massachusetts Inst. Technol., Cambridge, MA, USA, 2018.
- [32] A. V. Oppenheim and R. W. Schaffer, *Discrete-Time Signal Processing*, 3rd ed. Englewood Cliffs, NJ, USA: Prentice-Hall, 2002.
- [33] J. M. Bland and D. G. Altman, "Statistical methods for assessing agreement between two methods of clinical measurement," *Lancet*, vol. 327, no. 8476, pp. 307–310, 1986.
- [34] M. L. Daley *et al.*, "Plateau waves: Changes of cerebrovascular pressure transmission," *Acta Neurochirurgica Suppl.*, vol. 95, pp. 327–332, 2005.
- [35] M. H. Morgalla *et al.*, "ICP monitoring with a re-usable transducer: Experimental and clinical evaluation of the Gaeltec ICT/b pressure probe," *Acta Neurochirurgica (Wien)*, vol. 139, no. 6, pp. 569–573, 1997.
- [36] P. K. Eide, "Comparison of simultaneous continuous intracranial pressure (ICP) signals from ICP sensors placed within the brain parenchyma and the epidural space," *Med. Eng. Phys.*, vol. 30, no. 1, pp. 34–40, 2008.
- [37] T. Lescot *et al.*, "In vivo accuracy of two intraparenchymal intracranial pressure monitors," *Intensive Care Med.*, vol. 37, no. 5, pp. 875–879, 2011.
- [38] L. Zacchetti *et al.*, "Accuracy of intracranial pressure monitoring: Systematic review and meta-analysis," *Crit. Care*, vol. 19, no. 1, 2015, Art. no. 420.
- [39] J. C. O'Horo *et al.*, "Arterial catheters as a source of bloodstream infection: A systematic review and meta-analysis," *Crit. Care Med.*, vol. 42, no. 6, pp. 1334–1339, 2014.
- [40] K. B. Evensen *et al.*, "Non-invasive estimation of the intracranial pressure waveform from the central arterial blood pressure waveform in idiopathic normal pressure hydrocephalus patients," *Sci. Rep.*, vol. 8, no. 1, 2018, Art. no. 4714.
- [41] M. Ursino and C. A. Lodi, "A simple mathematical model of the interaction between intracranial pressure and cerebral hemodynamics," *J. Appl. Physiol.*, vol. 82, no. 4, pp. 1256–1269, 1997.
- [42] A. A. Linninger *et al.*, "A mathematical model of blood, cerebrospinal fluid and brain dynamics," *J. Math. Biol.*, vol. 59, no. 6, pp. 729–759, 2009.
- [43] V. Peterka, "Bayesian system identification," *Automatica*, vol. 17, no. 1, pp. 41–53, 1981.
- [44] B. Ninness and S. Henriksen, "Bayesian system identification via Markov chain Monte Carlo techniques," *Automatica*, vol. 46, no. 1, pp. 40–51, 2010.
- [45] D. Hori *et al.*, "Arterial pressure above the upper cerebral autoregulation limit during cardiopulmonary bypass is associated with postoperative delirium," *Brit. J. Anaesthesia*, vol. 113, no. 6, pp. 1009–1017, 2014.